Appl Phys B (2010) 98: 641–645
DOI 10.1007/s00340-009-3861-9

Applied Physics B
Lasers and Optics

Image formation in scanning electron microscopy of ultracold atoms

P. Würtz · T. Gericke · A. Vogler · F. Etzold · H. Ott

Received: 7 August 2009 / Revised version: 18 November 2009 / Published online: 12 February 2010

Abstract Imaging ultracold atoms by means of scanning electron microscopy involves several aspects that are different from standard optical imaging techniques. The quality of the images depends on the properties of the electron beam, and the signal depends on the details of the ionization process and subsequent detection strategy. We discuss the alignment and characterization procedure of the electron beam, the handling of different charge states that are produced upon electron impact, and correction algorithms to compensate for relative drifts between the field of view of the electron beam and the atomic target.

1 Introduction

The properties of ultracold quantum gases are usually studied using time of flight optical imaging techniques [1]. During the ballistic expansion the atoms interfere with each other, and the final momentum distribution contains information on the coherence and the density distribution of the gas. Small scale structures are transformed into high momenta and are therefore easy to detect while large scale structures lead to small momenta and are more difficult to identify. In situ optical imaging provides complementary information, and the density profile of the gas is directly visible [2]. However, in order to resolve small structures such as optical lattices, a high spatial resolution is mandatory [3–5].

Scanning electron microscopy applied to ultracold quantum gases constitutes an alternative in situ imaging technique that combines high spatial resolution with single atom sensitivity [6]. The signal generation is based on electron impact ionization of the trapped atoms with subsequent ion detection. Thereby, the scanning probe principle involves a sequential image formation, and the image reconstruction is performed by correctly assigning the detected events to the position of the electron beam. This relatively simple methodology is complicated by several aspects which we address in this article. We briefly introduce the working principle of the electron microscope in Sect. 2. The alignment procedure and the characterization of the electron beam is addressed in Sect. 3. The control of the target—especially in the context of long term drifts and short term fluctuations of its position—are detailed in Sect. 4. In the closing Sect. 5 we discuss the ion production and detection process and its influence on the image formation process.

2 Working principle

The working principle of the microscope is sketched in Fig. 1. A focussed electron beam intersects the atomic cloud which is prepared in a single beam optical dipole trap formed by a focussed CO_2 laser [7]. We produce thermal or Bose–Einstein condensed ensembles of ^{87}Rb atoms with about 10^5 atoms at a temperature of 80 nK. The elongated cloud is cylindrically symmetric and has a size of 6 µm × 100 µm. The electron beam is produced by an electron column, which is operated at 6 keV energy. The beam can be focussed to less than 100 nm full width at half maximum (FWHM) diameter and can be scanned in both transverse directions within a field of view of 1 mm × 1 mm. During the imaging procedure, the electron beam is scanned

P. Würtz · T. Gericke · A. Vogler · F. Etzold · H. Ott (✉)
Institut für Physik, Johannes Gutenberg-Universität,
55099 Mainz, Germany
e-mail: ott@uni-mainz.de

A. Vogler · H. Ott
Research Center OPTIMAS, Technische Universität
Kaiserslautern, 67663 Kaiserslautern, Germany

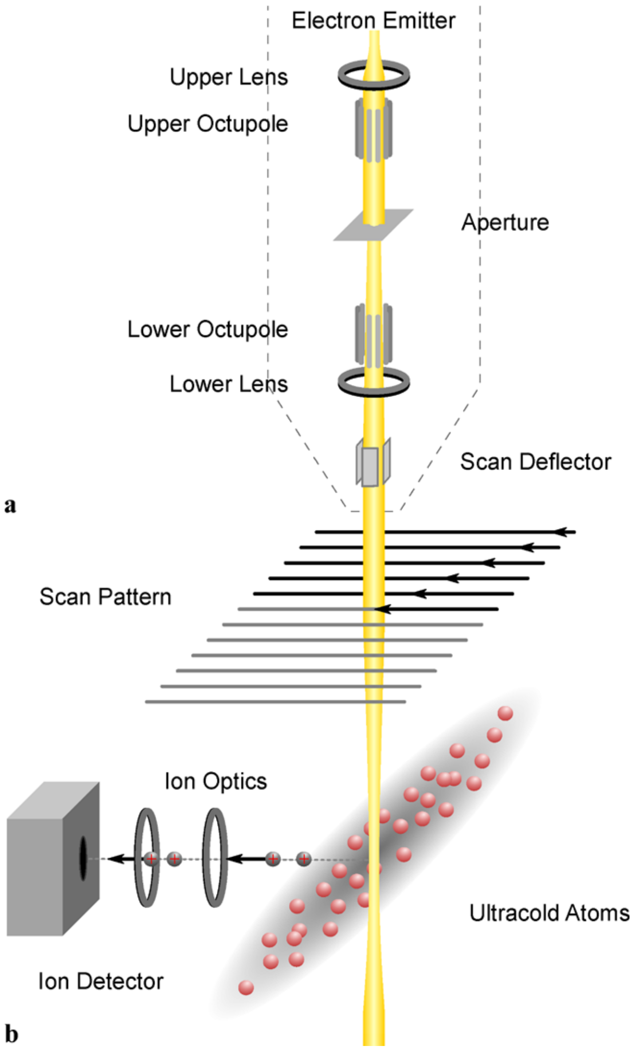

Fig. 1 Working principle of the microscope. A schematic view of the electron column, represented by *the dashed line*, is shown in the upper half of the figure (**a**). The elements are explained in the main text. (**b**) The column provides a focussed electron beam which intersects a cloud of ultracold atoms prepared in an optical dipole trap. Electron impact ionization produces ions which are guided by ion optics towards a detector

across the cloud and produces ions. An electrostatic field is applied in order to extract the ions and guide them towards a channeltron detector. A multi channel scaling card records the events from which the image is obtained. The spatial resolution of the imaging technique is set by the size of the electron beam. The scanning probe principle also allows for a local manipulation of the system which has recently been demonstrated by writing arbitrary patterns in a 2D optical lattice [6, 8].

3 Alignment and characterization of the electron beam

The electron column contains a thermal Schottky emitter and standard electron optics, consisting of two magnetic lenses, a variable aperture and a set of deflectors and stigmators (Fig. 1a). The electron beam is collimated by the first magnetic lens. Two deflector/stigmator units, each being realized as a single octupole element, are used to align the beam along the electron optical axis and to correct for astigmatism. The variable aperture is used to set the beam diameter inside column and the beam current. A second magnetic lens focusses the electron beam at a working distance of 13 mm below the tip of the electron column. Between both lenses, the electrons travel about 35 cm. The geometry of the lenses is such that the virtual electron source, which lies inside the emitter tip, is magnified at the position of the atoms by a factor of 4. Assuming a virtual source size of 20 nm [9], the FWHM beam diameter of the electron beam is about 80 nm. The real probe size can be substantially larger due to spherical aberration errors. Their influence can be reduced by inserting apertures into the beam, which decrease the beam's radial extension inside the column at the cost of beam current. The beam diameter may also be decreased by changing the excitation in both lenses to reduce the magnification. This leads to a more divergent beam between both lenses and an increase of spherical aberrations. Again, an aperture is required to compensate for this effect. The general trade-off between beam current and beam size is a common feature of all charged particle optics. Typical parameters that can be achieved with our present setup are summarized in Table 1.

Table 1 Typical working points for the electron column. The aperture is located behind the first magnetic lens and defines the radial extension of the beam inside the column. It influences the beam current and the contribution to the spot size stemming from spherical aberrations. The microscope is optimized for 6 keV electron energy, and the performance deteriorates with decreasing energy

	FWHM	Current	Aperture	Energy
#1	90 nm	12 nA	50 µm	6 keV
#2	250 nm	100 nA	100 µm	6 keV
#3	5 µm	800 nA	no aperture	6 keV
#4	400 nm	18 nA	50 µm	3 keV

Apart from the beam size and its shape, the quality of the field of view is of great importance. We perform a first adjustment by imaging the surface of a grid test target (Fig. 2a) which is mounted on a manipulator arm that can be moved inside the electron beam. The grid structure enables us to minimize astigmatism (Fig. 2c) and optimize the field of view (Fig. 2b). Scanning across the sharp edge of a hole target allows to determine the beam diameter.

One important difference of an electron imaging system compared to an optical technique is its large depth of focus. We verified this by changing the vertical position of the hole target and evaluating the edge spread function. Figure 3 shows the result for an electron beam with a FWHM

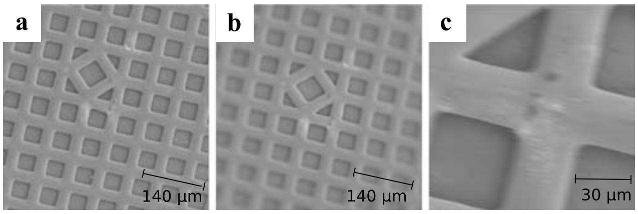

Fig. 2 Electron beam adjustment using the grid test target. Image (**a**) shows the test target after adjustment, whereas image (**b**) shows a low quality field of view caused by misaligned deflector elements. Image (**c**) is blurred horizontally due to astigmatism

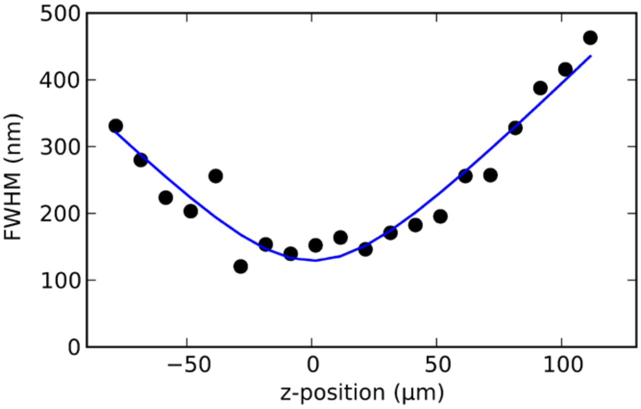

Fig. 3 Depth of focus of the electron beam. The diameter of the electron beam was measured for different positions of the hole target. The electron optics was left unchanged during the measurement

beam diameter of 120 nm. At larger distances, the size starts to increase linearly. Translated into the language of optics, the geometry of the electron beam focus corresponds to a Rayleigh length of 35 µm at a beam waist of 130 nm. Consequently, the size of the beam may be regarded as constant throughout the extension of the atomic cloud (6 µm).

After the first adjustment, the test target is removed and replaced by the optical dipole trap. Typically, the dipole trap is a few micrometers above or below the optimized working distance. This results in a larger and potentially astigmatic beam at the position of the dipole trap. Both effects are enhanced by the fact that the electrostatic field configuration changes when the test target is removed. Therefore, the fine adjustment of the electron beam has to be performed with the atomic cloud. In order to produce regular small structures in the cloud, we load the atoms in a 2D optical lattice with 600 nm period in each direction [6, 8]. Figure 4a shows an image of a Bose–Einstein condensate in the 2D lattice potential. In each experimental run we obtain one image that contains up to 4000 detected ions. By analyzing these images we determine the lattice contrast, and optimize it by changing the setting of the stigmator and refocussing the electron beam.

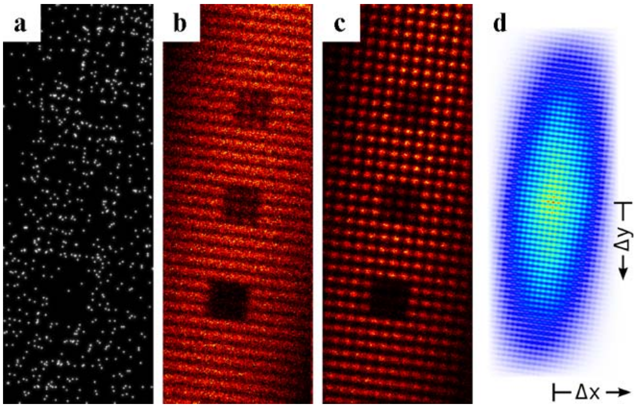

Fig. 4 (**a**) Single image (120 ms exposure time) from a sequence of 2D-lattice images. Prior to the scanning process, three blocks of lattice sites have been partially emptied by the electron beam. Image (**b**) shows the blurred, uncorrected sum of the image sequence. After phase correcting the single images, the summed image (**c**) shows no blurring, and the prepared block structures are preserved. The summed autocorrelation functions of multiple single images is shown in figure (**d**)

4 Lattice drifts and motion compensation

In many experiments, the spatial density distribution of an atomic ensemble is of great interest. In our typical scanning procedure, only a fraction of atoms is ionized and detected [6]. We therefore have to accumulate the images from many experimental realizations in order to increase the signal. In the case of optical lattices, the sum of the data may result in a blurred image, if the lattice exhibits slow drifts or unpredictable fluctuations. We can compensate for shot-to-shot movement in a postprocess similar to digital image stabilization algorithms [10]. This is done by identifying traceable features and their positions within consecutive images and cancel out movement by shifting the images. In our application, these features are the sites of the optical lattice. Their positions are determined by the phases $\phi_{1,2}$ of the two standing waves formed by the counterpropagating lasers. To this end, we need to analyze the lattice structure and determine the phases for each image.

A two-dimensional lattice structure can be described by two lattice translation vectors $\ell_{1,2}$, pointing from one site to its next neighbors in each direction. These vectors are not necessarily perpendicular. The lattice may also be represented by two plane waves with wave vectors $\mathbf{k}_{1,2}$, which define the reciprocal lattice. The first step is to determine both wave vectors as good as possible. By calculating the discrete 2D autocorrelation function $A(\Delta x, \Delta y)$ for a given signal $d(x, y)$

$$A(\Delta x, \Delta y) = \sum_{x,y} d(x, y) d(x - \Delta x, y - \Delta y),$$

we can add up all images ignoring the inconstant phases. The result of this sum is an image with very low noise

(Fig. 4d) from which the wave vectors can be obtained by finding the two most prominent peaks in the Fourier spectrum. In the second step we retrieve the phases $\tilde{\phi}_{1,2}$ and an amplitude A from the complex Fourier components $\hat{f}(\mathbf{k}_{1,2}) = A\, e^{i\tilde{\phi}_{1,2}}$ of each single image. The amplitude may be used as a measure of contrast of the lattice. Since the window length of the Fourier transform is limited, the phases $\tilde{\phi}_{1,2}$ are generally not equal to the plane wave phases $\phi_{1,2}$. For typical image sizes, however, the approximation is valid within 1%. This error is small compared to the standard deviation caused by the limited amount of data for determining the phase, which is about 5%. Finally, we are able to correct the images by shifting them along the lattice translation vectors by $\frac{\tilde{\phi}_1}{2\pi}\ell_1 + \frac{\tilde{\phi}_2}{2\pi}\ell_2$. The sum of all images that was previously blurred due to lattice drifts (Fig. 4b) now results in an image with significantly improved quality (Fig. 4c).

For future applications, such as the preparation of single lattice sites, an online correction method may be desirable which eliminates the need of a post process. This could be achieved by imaging and phase-analyzing only a small area of the lattice before proceeding with the preparation. From numerical experiments we find that the accuracy in determining the position of the lattice is given by $\frac{\Delta\phi}{\pi} \approx \frac{1}{\sqrt{N}}$. For a desired accuracy of 5% one would need a signal consisting of at least 400 ions. Such an image could be taken on an outer part of the cloud and would require an imaging time of a few ten milliseconds. If the plane wave vectors are already known, the calculation of the Fourier components $\hat{f}(\mathbf{k}_{1,2})$ can be reduced to a limited amount of products and sums, which digital signal processors could handle within milliseconds. We estimate that an online correction is feasible within a time window of about 100 ms.

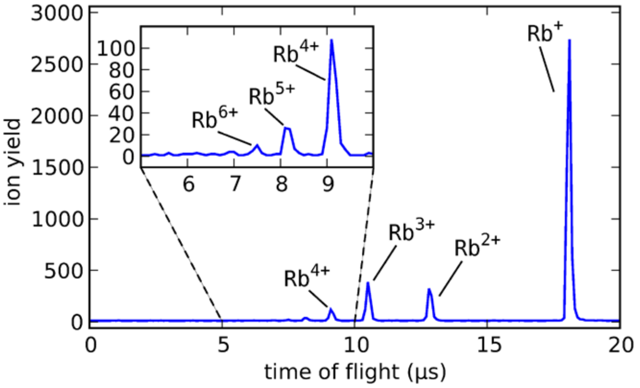

Fig. 5 Time of flight spectrum of ^{87}Rb atoms ionized by electron impact. The peaks in this spectrum correspond to the multiply charged states up to Rb^{6+}. About 80% of all detected ions are singly charged

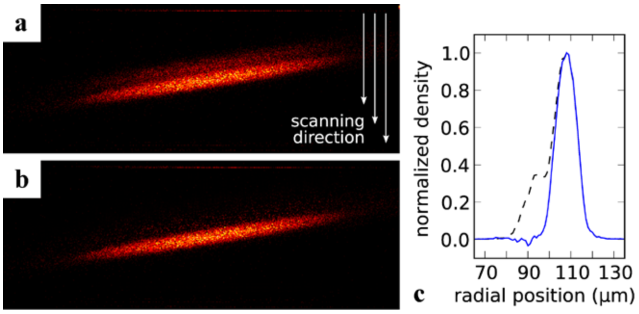

Fig. 6 Image of a BEC in an optical dipole trap being corrected for time of flight effects. Image (**a**) clearly suffers from multiply charged ions being attributed to incorrect pixels due to their different time of flight. The dwell time per pixel for this image is 0.5 μs. A corrected image (**b**) is obtained by recursively removing intensity from neighboring pixels. Figure (**c**) shows an integrated linescan along the trap axis of both images for comparison. *The dashed line* corresponds to the original image (**a**), whereas *the solid line* shows the profile of the corrected image (**b**)

5 Time of flight corrections

For mapping ion detection events to image coordinates, one needs to know the time of production of an ion and the position of the electron beam at this time. Apart from a negligible signal processing delay of about 160 ns, the time lag between ion production and detection is directly determined by the time of flight, which is $\Delta t_1 = 18$ μs for singly charged ^{87}Rb ions in our experimental setup. We therefore map a bin representing time t of the detection signal to the electron beam's position at $t - \Delta t_1$. This simple model is correct for most of the detection events, but about 20% of the produced ions are multiply charged, and their time of flight differs from the singly charged particles (Fig. 5). Since our detector cannot distinguish between these states, the time of production is estimated incorrectly for some ions, and they are attributed to preceding image pixels. Each multiply charged state adds an overlaying image, shifted according to its shorter time of flight (Fig. 6a). The amount of this shift is proportional to the scanning speed, thus it increases as the dwell time per pixel is reduced.

The detected signal can be understood as convolution of the number of ions $n(t)$ produced at time t and the time of flight spectrum. We denote the probability of producing an ion of charge state i as γ_i and its time of flight as Δt_i. The signal $\tilde{s}(t)$ may then be written as:

$$\tilde{s}(t) = \sum_i \gamma_i n(t - \Delta t_i).$$

Based on the information from the time of flight spectrum, we can approximate the undisturbed image by recursively removing fractions of counts attributed incorrectly. For convenience, we clip the first 18 μs from the signal so it is shifted by Δt_1:

$$s(t) = \tilde{s}(t + \Delta t_1) = \gamma_1 n(t) + \sum_{i=2} \gamma_i n\big(t + |\Delta t_1 - \Delta t_i|\big)$$

$$n(t) = \frac{1}{\gamma_1} s(t) - \sum_{i=2} \frac{\gamma_i}{\gamma_1} n\big(t + |\Delta t_1 - \Delta t_i|\big).$$

The unknown function $n(t)$ now depends on the signal $s(t)$ and on contributions of $n(t)$ from later times. If the ion production stops 18 µs prior to a specific moment $t_{\max}$

$$n(t) = 0 \quad \forall t > t_{\max},$$

the last ions detected must be singly charged, since the Rb^+ ions are the slowest particles to arrive. In this case no multiply charged ions contribute to the signal, and we directly obtain the number of ions produced at this specific time:

$$n(t_{\max}) = \frac{1}{\gamma_1} s(t_{\max}).$$

We are now able to calculate $n(t)$ reversely from $t_{\max}$ to $t = 0$ since the recursion ends within $n(t)$. Beginning at $t_{\max}$, a fraction $\frac{\gamma_i}{\gamma_1}$ from the signal bin $s(t)$ is subtracted from a preceding bin $s(t - |\Delta t_1 - \Delta t_i|)$. This preceding bin is now cleared from the specific charged state i and should be clear of all multiply charged states once the algorithm proceeded to the bin. The result of this postprocessing method is shown in (Fig. 6b). Although some noise has been transferred from the real density-distribution signal to the area where the duplicated image was, the time of flight artifact is considerably reduced. Figure 6c shows two linescans for comparison. The dashed line corresponds to the original image, whereas the solid line shows the profile of the corrected image.

6 Conclusions

In summary, we have described the details of the image formation process in scanning electron microscopy applied to ultracold quantum gases. The peculiarities of this technique involve several complications that can be addressed by properly designed alignment and compensation schemes. The technique is now well established and quantitatively understood. In the future, we expect to gain new insights into the microscopic structure of quantum gases by high precision, high resolutiont in situ measurements.

Acknowledgement We gratefully acknowledge financial support from the DFG under Grant No. Ot 222/2-3.

References

1. W. Ketterle, D.S. Durfee, D.M. Stamper-Kurn, in *Bose–Einstein Condensation in Atomic Gases. Proceedings of the International School of Physics "Enrico Fermi", Course CXL*, ed. by M. Inguscio, S. Stringari, C.E. Wieman (IOS Press, Amsterdam, 1999)
2. M.R. Andrews, M.-O. Mewes, N.J. van Druten, D.S. Durfee, D.M. Kurn, W. Ketterle, Science **273**, 84 (1996)
3. K.D. Nelson, X. Li, D.S. Weiss, Nature Phys. **3**, 556 (2007)
4. M. Karski, L. Förster, J.-M. Choi, W. Alt, A. Widera, D. Meschede, Phys. Rev. Lett. **102**, 053001 (2009)
5. M. Albiez, R. Gati, J. Fölling, S. Hunsmann, M. Cristiani, M.K. Oberthaler, Phys. Rev. Lett. **95**, 010402 (2005)
6. T. Gericke, P. Würtz, D. Reitz, T. Langen, H. Ott, Nature Phys. **4**, 949 (2008)
7. T. Gericke, P. Würtz, D. Reitz, C. Utfeld, H. Ott, Appl. Phys. B **89**, 447 (2007)
8. P. Würtz, T. Langen, T. Gericke, A. Koglbauer, H. Ott, Phys. Rev. Lett. **103**, 080404 (2009)
9. J. Orloff, *Handbook of Charged Particle Optics* (CRC Press, Boca Raton, 1997)
10. M. Tico, M. Vehvilainen, *Proc. of 3rd ISCCSP* (2008)